Fusion welding of nickel–titanium and 304 stainless steel tubes: Part I: laser welding

Ryan Hahnlen, Gordon Fox and Marcelo J Dapino

Abstract

Due to their large blocking stresses, high recovery strains, and solid-state operation, nickel–titanium actuators can offer substantial weight and space savings relative to traditional electric or hydraulic systems. A challenge surrounding NiTi-based actuators is integration of the NiTi components into a given system; this alloy is difficult and expensive to machine and challenging to weld to itself and structural materials. In this research, we join NiTi and 304 stainless steel tubes of 9.53 mm (0.375 in) in diameter through laser welding to create joints with weld depths up to 1.65 mm (0.065 in). By joining NiTi to a common structural material that is easily machined and readily welded to other materials, system integration is greatly improved. The joints prepared in this study were characterized through optical microscopy, hardness mapping, energy dispersive X-ray spectroscopy, mechanical testing, and analysis of the resulting fracture surfaces. The average ultimate shear strength of these joints is 429 MPa (62.2 10^3 lbf/in^2) and the resulting fusion zone has a maximum width of 21.9 μm with a maximum hardness of 929 HV, while a possible heat-affected zone in NiTi is limited between 1 and 2 μm over most of the weld.

Keywords

Shape memory, manufacturing, system integration, NiTi welding, shape memory alloys

Introduction

Nickel–titanium (NiTi) is a shape memory alloy capable of recovering large deformations, up to 8%, and exerting large forces as it undergoes a temperature-induced transformation from its martensite to austenite phase (Johnson Matthey, 2011; Nitinol Devices & Components, 2009). These properties make NiTi a desirable material for use in lightweight actuators capable of reliable solid-state operation.

NiTi-based actuators have been successfully used to bend a chevron on the trailing edge of a jet engine fairing into the exhaust stream, improving the mixing characteristics of the boundary layer and reducing engine noise (Hartl et al., 2008). The small size, relative simplicity, and ruggedness of these actuators also make them strong candidates for torsional actuators to be inserted into helicopter rotor blades that optimally change their twist profile depending on flight conditions (Mabe et al., 2004). However, the broad implementation of NiTi in commercial products has been hindered by the difficulties in integrating these alloys into mechanical systems.

Machining NiTi is difficult due to its high ductility, work hardening characteristics, and nonlinear stress–strain behavior. These characteristics often cause chatter, poor surface finish, irregular chip breakage, and high tool wear (Weinert and Petzoldt, 2004). The build-up of heat in traditional machining processes can also locally affect thermomechanical properties of the NiTi workpiece, reducing the magnitude and repeatability of the shape memory effect (Wu, 2001). Electric discharge machining is commonly used to create NiTi parts, although this process is relatively slow and expensive when compared with traditional machining processes. Much of difficulty and expense associated with integrating NiTi into structures can be eliminated if a reliable and efficient way of joining it to traditional structural materials, such as steel alloys, is developed. A key issue is that joining NiTi to itself and, particularly, to dissimilar materials presents several challenges.

Smart Materials and Structures Laboratory, Department of Mechanical and Aerospace Engineering, The Ohio State University, Columbus, OH, USA

Corresponding author:
Marcelo J Dapino, Smart Materials and Structures Laboratory, Department of Mechanical and Aerospace Engineering, The Ohio State University, Columbus, OH 43210, USA.
Email: dapino.1@osu.edu

Although adhesives can be used to join NiTi to other materials, the resulting joints suffer from limited strength, degrade over time, and are generally not biocompatible (Hall, 1999). Soldering has been successfully accomplished either using aggressive fluxes (Hall, 1993) or ultrasonically vibrating soldering irons. Similar to adhesives, large contacting surface areas are required to obtain high-strength joints, which constrain significant portions of the active NiTi component (Hahnlen et al., 2012). Despite the several challenges associated with welding NiTi to itself or other materials, this process holds the most promise for producing consistent, high-strength joints.

When fusion welding NiTi, there are two main concerns. The first is the loss of cold work and material training. Welding can degrade the shape memory and superelastic effects of the NiTi components due to excessive heating. It is possible to regain some of the original properties through postweld heat treatments and additional training, but this adds cost and complexity to the joining process (Wang, 1997).

The second concern in welding NiTi is the formation of brittle intermetallic compounds. Fusion welding NiTi to itself can result in solidification or "hot cracking." Hot cracking occurs due to the solidification temperature range of an alloy. As the molten NiTi in a weld pool cools through its solidification range, a network of solid alloy forms in the liquid portion of the weld pool. The liquid is typically $TiNi_2$, which solidifies into a brittle compound. When the solidifying weld pool begins to form grain structures, the liquid $TiNi_2$ infiltrates the grain boundaries. As the liquid cools and solidifies, the additional shrinking leaves cracks at the grain boundaries. These cracks can propagate through the weld and cause joint failure. In severe cases, the weld may fail completely even before it is cooled (Cieslak, 1993; Wang, 1997).

"Cold cracking" is a phenomenon that occurs when joining titanium alloys to ferrous alloys. The titanium and iron form brittle intermetallic compounds, such as TiFe and $TiFe_2$, which have low strength at room temperature (Wu, 2001). Fusion welding NiTi to steel readily creates intermetallics that form along the weld line (Van der Eijk et al., 2003). The contracting volume of the workpiece places the intermetallics under stress and causes cracks to propagate during cooling. These cracks often result in total weld failure as the joint cools to room temperature. As described by Hall (2005), a NiTi/ferrous alloy weld can be successfully made with Ni-rich filler metal. The addition of Ni dilutes the weld pool, reducing the relative amount of molten Ti and Fe in the joint, hence avoiding the formation of intermetallic compounds. By adding more Ni to the weld pool, there is also a reduction in hot cracking due to relative reduction of molten Ti.

This research focuses on fusion welding NiTi to 304 stainless steel (304 SS) tubes for use in torsional solid-state actuators. This particular stainless steel alloy was chosen as the structural material because it is widely used and is easy to machine and weld (AK Steel Corporation, 2007). The tubular geometry was used in this study to simulate the geometry of a torsional actuator. When torque is applied, tubes have a more consistent shear stress across their cross section than solid rods, which aids the analysis of the shear properties of these joints. Tubes also have a higher strength and stiffness-to-weight ratio than solid rods, which is especially important in aerospace applications where weight must be minimized. The research is presented in two parts with each part focusing on a different fusion welding method. Part I focuses on laser welding in which the base metals are melted via a pulsed laser, while Part II investigates tungsten inert gas (TIG) welding, which utilizes an electric arc to heat and melt the base metals.

To create viable fusion welds between NiTi and 304 SS, the two main challenges, loss of cold work and training as well as intermetallic formation, must be addressed. Part I of this study combines laser welding and the use of Ni-rich filler metal to create multiple tubular joint geometries between NiTi and 304 SS. Laser welding intrinsically avoids loss of cold work due to the focused nature of the heat source, which results in a narrower heat-affected zone (HAZ) and less thermally affected material. This characteristic of laser welding helps to alleviate the loss of shape memory properties without the need for postweld treatments. NiTi has been successfully welded to itself (Falvo et al., 2005; Kahn et al., 2008) and to dissimilar metals (Gugel et al., 2006) using this process with little loss of shape memory or superelastic properties. The use of Ni-rich filler metal suppresses intermetallic formation, thus allowing the creation of viable samples. The resulting joints were characterized through optical microscopy, hardness testing, composition analysis via energy dispersive X-ray spectroscopy (EDS), mechanical testing to determine their torsional strength, and analysis of the resulting fracture surfaces using scanning electron microscopy (SEM).

Experimental procedure

Sample construction

Three types of joints, differing by their diameters and wall thicknesses, were created. All were welded using a neodymium-doped yttrium aluminum garnet (Nd:YAG) laser. The Ni-rich filler metal was commercially pure nickel (Ni 200), which took different forms as needed for each type of joint. To avoid reactions with oxygen, nitrogen, or other atmospheric contaminants, argon was used as a shielding gas in all cases.

The first joint geometry utilized small diameter NiTi and 304 SS tubes with outer diameters of 5.08 mm

(0.200 in) and wall thicknesses of 813 μm (0.032 in). Filler material was provided with a Ni washer 381 μm (0.015 in) thick held between the tubes on a tungsten mandrel to keep all the components aligned and in place during welding, as seen in Figure 1(a) and (b). These pilot samples were used to determine the maximum single-pass weld penetration attainable with the laser system. The joints were created by rotating the sample as the laser pulsed. A completed pilot sample is shown in Figure 1(c). These joints were sectioned for optical microscopy to observe weld penetration and observe the overall structure of the weld. For each pilot trial, the spot size, peak power, and pulse frequency were fixed at 1.1 mm, 1.8 kW, and 0.7 pulses per second (pps), respectively, while total pulse energy was varied by changing pulse duration. Parameters for these joints are presented in Table 1.

A second set of joints was created utilizing tubes with a diameter of 9.53 mm (0.375 in) and wall thickness of 381 μm (0.015 in), which is shown in Figure 2(a). The Ni filler used in these joints was in the form of pre-placed unions, which are shown in Figure 2(b). The welding setup is shown in Figure 2(c). Five total samples were made, four of which were tested for torsional strength, while the fifth was sectioned and polished to observe the weld penetration and weld structure. For each trial, the spot size, peak power, and pulse frequency were fixed at 0.7 mm, 1.1 kW, and 1.3 pps, respectively. Pulse energy was varied by adjusting pulse duration. All these parameters can be seen in Table 1. Thin-walled samples 3, 4, and 5 have the same weld parameters, as discussed later.

A third set of samples was created by using 9.53-mm-diameter NiTi and 304 SS tubes with a wall thickness of 1.65 mm (0.065 in). This set of joints was created by machining a 45° bevel on the mating end of each tube and making multiple weld passes to fill the groove, similar to the methods for creating large-scale pipe welds. This geometry is shown in Figure 3. The Ni filler for this joint configuration was hand-fed Ni wire 254 μm (0.010 in) in diameter when welding the root passes and Ni wire 508 μm (0.020 in) in diameter for welding the fill passes. A total of four thick-walled samples were created, three of which were used for optical microscopy and one was tested for torsional strength. Since this welding process required multiple passes, more heat was applied to the NiTi tube in the thick-walled joints. For this reason, along with possible variation due to hand-feeding the Ni filler, most of the samples were used for optical microscopy to observe possible weld defects and variations in the weld structure. Two sets of parameters were used in creating each thick-walled sample, one for the initial root pass and the other for subsequent fill passes. The spot size was set at 0.4 mm for the root passes and 0.75 mm for fill passes. Pulse frequency for each pass was fixed at 5 pps. All parameters for both passes are shown in Table 1.

All laser joints were made in conduction mode, in which the base metals are heated beyond their melting point via thermal conduction. Higher powers can be used to generate deeper welds in keyhole mode, involving vaporization of the base metals to allow the laser to heat metal deeper within the fusion zone. Keyhole laser welding was avoided for two reasons: the vaporization of the base metals can result in void inclusions and keyhole mode produces high weld aspect ratios making the inclusion of filler metal difficult. For these reasons, conduction mode was determined to be the most suitable procedure for fabricating the NiTi/304 SS welds.

Optical microscopy, hardness testing, and EDS

All pilot samples, thin-walled sample 5, and thick-walled samples 1–3 were sectioned and polished to study the cross section of the welds. Several regions are observed. While autogenous weld joints have three primary regions, unaffected base metal, a HAZ, and a fusion zone or homogeneous weld pool, the samples in this study are different due to the dissimilar nature of the base metals and the use of filler metal, giving rise to additional regions. For the following analyses in both Part I and Part II, the regions will be identified as either base metal, HAZ, fusion zone/weld pool, partially mixed zone, or unmixed zone. An aspect of dissimilar welds is that the weld pool itself is not a homogeneous region but rather a mix of multiple regions of different compositions (Kou, 2003). Within the fusion zone/weld pool, there may be multiple partially mixed zones differentiated by their compositions. The discussion of partially mixed zones in this work is limited to those observed within the NiTi fusion zone of the observed welds. In addition to these regions, nickel alloys may also exhibit an unmixed zone, a region along the fusion boundary where the nickel-alloy base metal became liquid but did not mix with the rest of the weld pool

Table 1. Laser parameters for NiTi/304 SS sample construction.

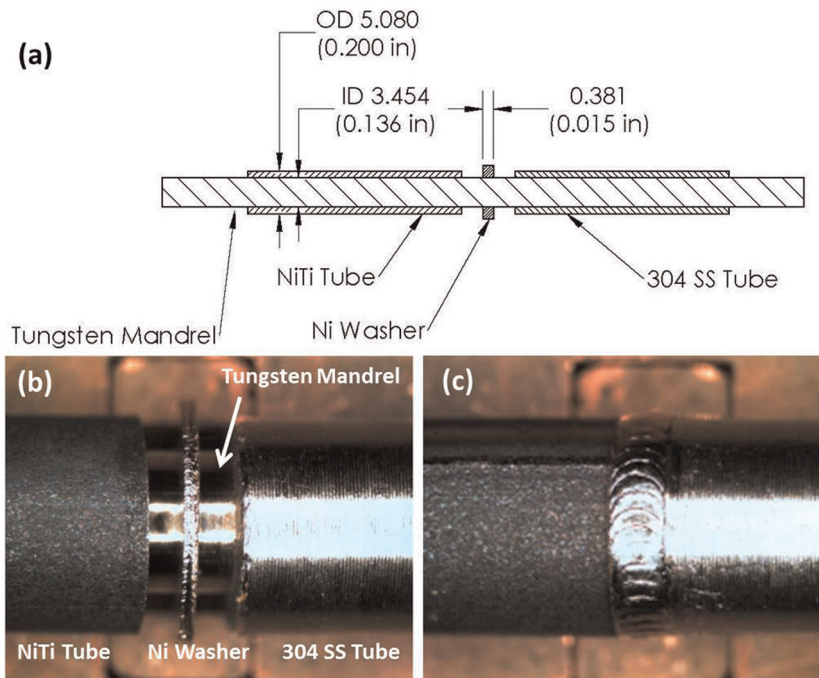| Type	Weld	Spot size (mm)	Frequency (pps)	Power (kW)	Pulse duration (ms)	Energy (J)
Pilot test	1	1.10	0.7	1.80	9.8	17.6
	2	1.10	0.7	1.80	12.0	21.6
	3	1.10	0.7	1.80	14.0	25.2
Thin walled	1	0.70	1.3	1.25	14.0	17.5
	2	0.70	1.3	1.15	13.0	15.0
	3	0.70	1.3	1.10	13.0	14.3
	4	0.70	1.3	1.10	13.0	14.3
	5	0.70	1.3	1.10	13.0	14.3
Thickwalled	Root	0.40	5.0	0.52	3.4	1.8
	Fill	0.75	5.0	1.00	13.0	13.0

Figure 1. (a) Exploded diagram of NiTi/304 SS pilot laser weld, (b) pilot joint assembled preweld, and (c) laser pilot weld.
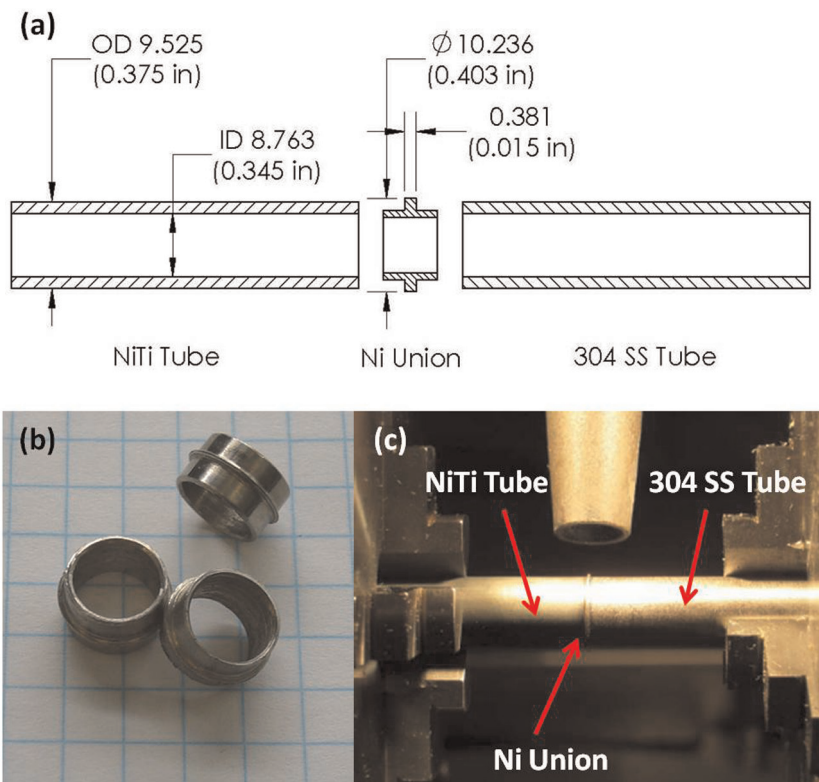

Figure 2. (a) Exploded diagram of thin-walled laser weld, (b) Ni union used for filler metal, and (c) assembled specimen in welding fixture.

(Tillack, 1993). In dissimilar welds, partially mixed zones and unmixed zones (if present) are regions that were liquid during the welding process. For this reason, the fusion boundary is taken as the boundary between the weld pool and HAZ or unmixed zone and HAZ, if applicable.

Optical microscopy studies were first conducted to observe the overall structure of the welds. Through

microscopy, the weld penetration is observed as a lightly shaded region adjacent to and running parallel with the fusion boundary in the NiTi portion of the sample. These regions, further discussed in the following section, are believed to be a combination of partially mixed zones and the HAZ and are termed the affected zone for the optical microscopy studies. Weld penetration and affected zone width were measured using ImageJ (US National Institutes of Health, 2009), an image-processing program.

In addition to observing weld penetration and the affected zones, hardness maps were made from thin-walled sample 5 and thick-walled sample 2. The hardness maps were constructed by making a series of indents with a diamond indenter and 25 g load spaced 70 μm (0.003 in) in both the axial (x-axis) and radial (y-axis) directions for thin-walled sample 5 and 130 μm (0.005 in) in the axial and radial directions for thick-walled sample 2. These maps were used to determine bulk NiTi hardness and observe variation in hardness due to possible intermetallic formations and large-scale HAZ formation not observed through optical means. To augment the hardness maps and investigate the affected zone observed in the optical micrographs, individual hardness tests were conducted using a diamond indenter and 50 g load.

After hardness testing, thin-walled sample 5 and thick-walled sample 2 were placed in an SEM for the EDS analysis. In selecting the regions for the EDS testing, the backscatter detector of the SEM was used to aid in identifying regions of different compositions. The EDS measurements augment the hardness maps, identifying the composition of regions of hardness changes to

determine whether the hardness change is due to thermally induced changes in the grain structure, such as with a HAZ, or due to changes in composition and formation of intermetallic compounds.

Since one of the primary concerns with NiTi/ferrous alloy welding is cracking due to Ti–Fe intermetallic formation, the critical area for these joints is identified as the NiTi fusion zone. This is reinforced by the common failure point along the NiTi fusion boundary for all samples as described in the following sections. For this reason, the composition analysis has only been performed on the NiTi portion of these welds.

Mechanical testing and fracture surface analysis

Thin-walled samples 1–4 and thick-walled sample 4 were used for mechanical testing to observe the ultimate torsional strength of the welds. For all tests, a torsional testing system, as shown in Figure 4, was used to apply an angular displacement ramp at a rate of approximately 0.5°/s. Samples were loaded until failure, while the applied torque was measured with a reaction torque cell, and the angular displacement of the specimens was measured using an optical angular encoder. For each test, clamp grips were used to fixture the specimen. The edge of the grips was placed 6.35 mm (0.25 in) from the centerline of the weld, so that each test had the same length of NiTi and 304 SS tube deflecting with applied load.

After mechanical testing, the NiTi fracture surface of thin-walled sample 2 and thick-walled sample 4 was examined using an SEM. The samples were first cleaned through a methanol rinse and allowed to dry at room temperature.
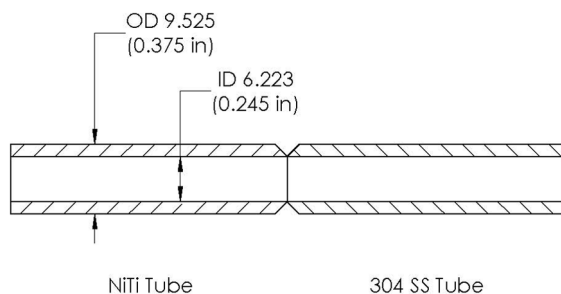
Results and discussion

Sample construction

The sectioned pilot samples do not show instances of cracking at the toes or faces of the welds. This indicates that there was sufficient Ni-rich filler metal to dilute the weld pool and avoid the formation of Ti–Fe intermetallics. There is no discoloration of the base metals, as shown in Figure 1(c), which would be an indication of overheating and subsequent loss of cold work.
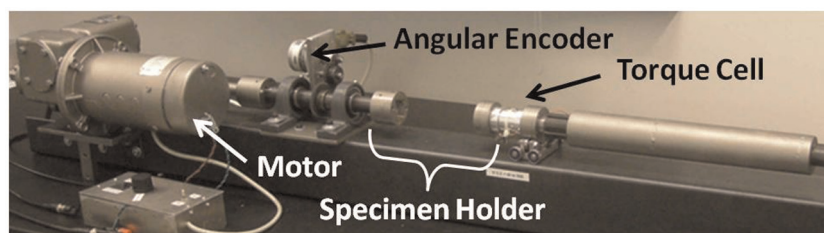

Figure 3. Diagram of thick-walled laser weld.

Figure 4. Torsion system used for mechanical testing of thin- and thick-walled NiTi/304 SS laser-welded samples.

The welded thin-walled samples are shown in Figure 5. In thin-walled sample 1, the 304 SS portion has a discolored region, which is highlighted in the inset. This is an indication of excessive heating of the joint. Subsequent thin-walled samples were made with lower pulse energies to avoid overheating of the base metals. From Table 1, samples 3–5 were constructed using the same parameters. This is because in creating sample 3, a pinhole defect was observed in the weld bead. The defect is likely due to surface contamination on either the base metal or the Ni insert. To obtain a surface-defect-free joint with the same parameters, sample 4 was made. Sample 5 was made to observe the microsection resulting from the parameter set used in samples 3 and 4.

Completed thick-walled samples, as shown in Figure 6, have no visible surface defects. The slight differences in bead formation are due to hand-feeding the Ni filler wire during welding. Initial root passes in the thick-walled joints were crack sensitive and occasionally cracked as the weld cooled. The subsequent fill passes became much less crack sensitive. This is believed to be due to the proximity of the NiTi and 304 SS tubes at the root and the relatively small size of Ni filler that was used for the root pass. As fill passes continue, the groove geometry provided greater separation of NiTi and 304 SS, thereby reducing the risk for Ti–Fe intermetallic formation.

Figure 5. Completed thin-walled NiTi/304 SS specimens; inset: detail of weld region in sample 1 showing discoloration indicative of excessive base metal heating.

Figure 6. Completed thick-walled NiTi/304 SS specimens.

The depth of the joint in the thick-walled samples represents a method of overcoming the primary limitation of laser welding in conduction mode, relatively shallow weld penetration. By using multiple passes, the joint depth is essentially unlimited. To decrease the time required to create such joints and increase repeatability, the wire feed process could be automated for future joints.

Optical microscopy

Optical microscopy of the pilot samples reveals an average weld penetration of 457 μm (0.018 in). In the micrographs, the affected zone is also present, a lighter shaded region in the NiTi base metal adjacent to the fusion boundary, as shown in Figure 7. This region is visible in all pilot samples and is believed to consist of partially mixed zones and the HAZ in the NiTi tube. Using ImageJ, the width of this region was measured at several points along the NiTi boundary of the weld pool. The average of these measurements for each sample and the maximum weld penetration are reported in Table 2.

The pulse energy of the laser can be estimated by multiplying the peak power by the pulse duration for each sample. In order to attain greater penetration, more energy must be applied to the joint. While the ideal weld would have full penetration and a small affected zone, these are conflicting objectives. In comparing the pulse energy to the penetration measured in the pilot samples in Table 2, there is little increase in penetration as pulse energy increases, but there is a significant increase in the width of the optically observed affected zone. For this reason, the pulse energy in pilot sample 1 is preferred and was used as a starting point in creating the thin-walled joints.

A micrograph of thin-walled specimen 5 is shown in Figure 8(a). Penetration extends into the annular cylinder of the Ni union, as expected from the average penetration of the pilot tests. A lighter shaded region, believed to be the affected zone, is observed in the NiTi
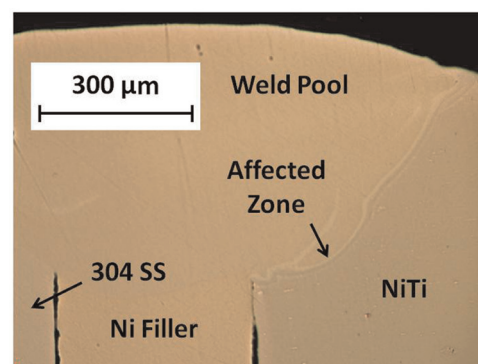

Figure 7. Micrograph of laser pilot weld after sectioning and polishing.

region adjacent to the weld pool. The average width of this region is 7.90 μm (3.11×10⁻⁴ in), which falls within the range of values observed in the pilot samples.

The widths of the affected zones observed in the thick-walled sectioned samples are compared to that of thin-walled sample 5 in Table 3. The thick-walled specimens have full thickness weld penetration, 1.65 mm, as designed by the joint setup and weld procedure, and an average affected zone extension of 21.9 μm (8.62×10⁻⁴ in). This is wider than the optically identified affected zone in the pilot and thin-walled joints. However, the increase in width is expected as multiple weld passes cause increased heating of the base metals with each successive pass.

The thick-walled joint sections show that although some cracking in the root pass was observed during welding, subsequent welds remelted the root pass and further diluted the weld pool, which prevented the reformation of the cracks. This can be seen in Figure 8(b). The micrographs of the thick-walled joints show voids in some welds. The voids are characterized as round or oblong dark areas in the sections and are differentiated from cracks by the smooth corners as opposed to sharp jagged features seen in crack formations. The voids are due to contaminants in the weld from either the tube-beveling process or the hand-fed Ni-rich filler wire. As the joint is heated to create fusion of the base metals, the contaminants vaporize and produce a gas bubble within the solidifying weld pool (Hobart Institute of Welding Technology, 2009). While such a defect would not be acceptable in production welds, it is easily remedied by ensuring all workpieces and filler material are thoroughly cleaned prior to joining.

Hardness testing

The hardness map created from thin-walled sample 5 is shown in Figure 9. The dashed lines in the figure represent the fusion boundaries between the weld pool and base metals as approximated from Figure 8. On the right portion of the map, there is a lighter shaded region that corresponds to the boundary of the weld pool and NiTi tube. In this region, the map shows a contiguous region of increased hardness, between approximately 400 and 850 HV. To the right of the light-shaded region is the NiTi tube, which has a hardness range of approximately 200–350 HV. This hardness value is typical of NiTi (Alapati et al., 2006) and indicates that the material in this region is unaffected by the heat generated by the welding process. The variation in hardness of the bulk NiTi is likely due to different orientations of the martensitic variants or Ni-rich intermetallics in the as-received material.

A similar map made from thick-walled specimen 2 is shown in Figure 10. The NiTi tube to the far right has a hardness that ranges from 200 to 350 HV. There is a region near the NiTi portion of the joint adjacent to the fusion boundary that has isolated hardened areas, but no continuous HAZ, which would appear as a continuous region of decreased hardness.

While the hardness maps do indicate regions of increased hardness in the weld immediately adjacent to the fusion boundaries, the spacing of the measurement points is too wide to measure the hardness of the regions identified through optical microscopy. In order to investigate the optically identified regions and determine whether they constitute either the NiTi partially

Table 2. Laser weld penetration and pulse energy of pilot NiTi/304 SS samples.

Weld	Depth, μm (in)	Affected zone width, μm (in)	Pulse energy, J
1	432 (0.017)	7.01 (2.76×10⁻⁴)	17.6
2	432 (0.017)	10.7 (4.21×10⁻⁴)	21.6
3	483 (0.019)	13.0 (5.12×10⁻⁴)	25.2

Table 3. Average HAZ extension observed in NiTi/304 SS samples.

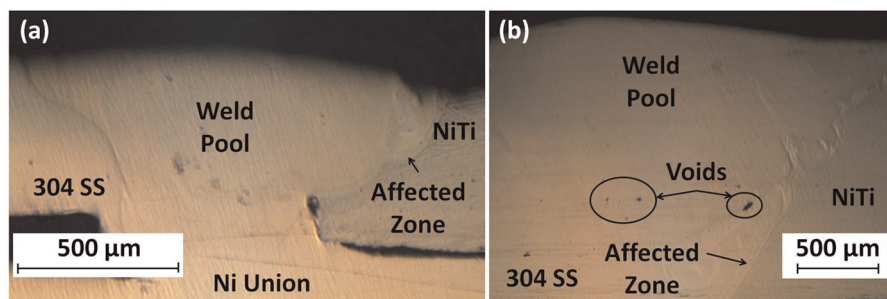| Sample	Affected zone width, μm (in)
Thin-walled 5	7.90 (3.11×10⁻⁴)
Thick-walled 1	19.2 (7.56×10⁻⁴)
Thick-walled 2	24.4 (9.61×10⁻⁴)
Thick-walled 3	22.2 (8.74×10⁻⁴)

HAZ: heat-affected zone.

Figure 8. Micrograph of (a) thin-walled NiTi/304 SS specimen 5 and (b) thick-walled NiTi/304 SS specimen 2.

mixed zone or HAZ, additional hardness indents were created. The additional measurements taken on thin-walled specimen 5 are shown in Figure 11. Two indents are completely within the optically identified affected zone, indicated for clarity by the dashed curved lines. For reference, a single indent was made in both the bulk NiTi and the solidified weld pool. The NiTi indent has a hardness of 213 HV and is 37 μm from the weld pool boundary. Both indents within the affected zone have significantly higher hardness values, 929 and 898 HV. From a weld pool indent close to the affected zone boundary, the hardness drops to 521 HV. Both indents outside the affected zone indicate that the hardness observed in the affected zone is limited to the region observed through optical microscopy.

A similar analysis was conducted on thick-walled specimen 2. Two indents were made within the optically identified affected zone and have hardness values of 801 and 757 HV, as shown in Figure 12. A reference indent in the bulk NiTi 22 μm away from the weld line has a hardness of 278 HV, indicating that the affected region is within the limits identified through optical microscopy. An explanation for the observed increased hardness in the affected region is discussed further in the following section. In both the thick- and thin-walled hardness measurements, the regions of increased hardness, and likely degradation of shape memory properties, is limited to a narrow region at the weld interface. Because of this, the welding process should have little effect on the total shape memory effect of the NiTi tube.
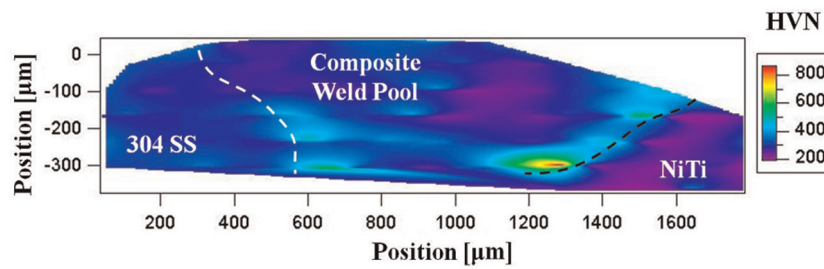

Figure 9. Hardness map of NiTi/304 SS thin-walled laser weld specimen 5. Dashed lines indicate approximate fusion boundaries.
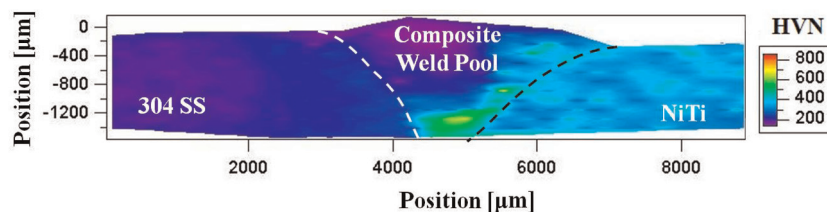

Figure 10. Hardness map of NiTi/304 SS thick-walled laser weld specimen 2. Dashed lines indicate approximate fusion boundaries.
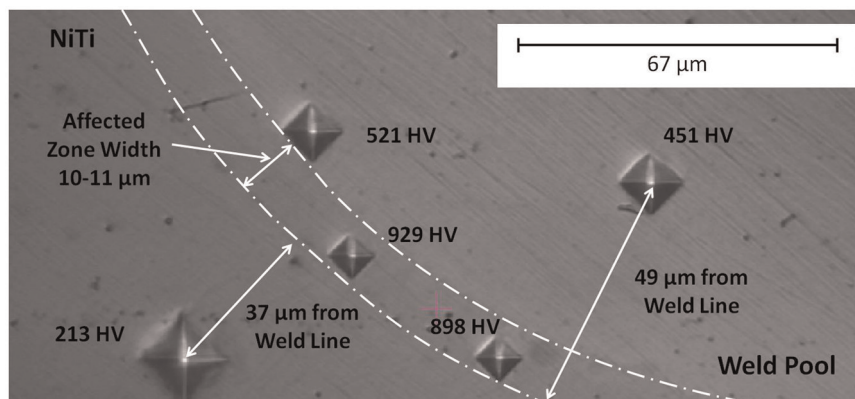

Figure 11. Individual hardness measurements in optically identified affected zone of NiTi/304 SS thin-walled specimen 5. The increased hardness is due to the formation of intermetallic compounds.

EDS analysis

Thin-walled sample 5 was found to have 5 distinct regions spanning from the bulk NiTi tube to the weld pool. These regions are indicated in Figure 13. Region 1 is the bulk NiTi material as determined from its similarity in composition as compared to an analysis region taken at the far end of the tube. Region 2 is a narrow line that runs along the entire weld interface with a typical width of less than 1 μm. While the typical width of this region is too small for the EDS measurements with the available equipment, near the root of the weld this

region becomes wide enough to conduct an analysis. Region 3 is the same region that is observed in the optical micrographs and shares an irregular boundary with regions 2 and 4. The fourth region is taken as a representation of the weld pool, as no contiguous distinction between it and the weld bead can be made. Region 5 is a lighter shaded inclusion within region 4 not previously identified through optical means.

The nature of each region was determined by its shared boundary with other adjacent regions and composition. The composition results can be seen in Table 4. Regions 1 and 2 have similar composition to
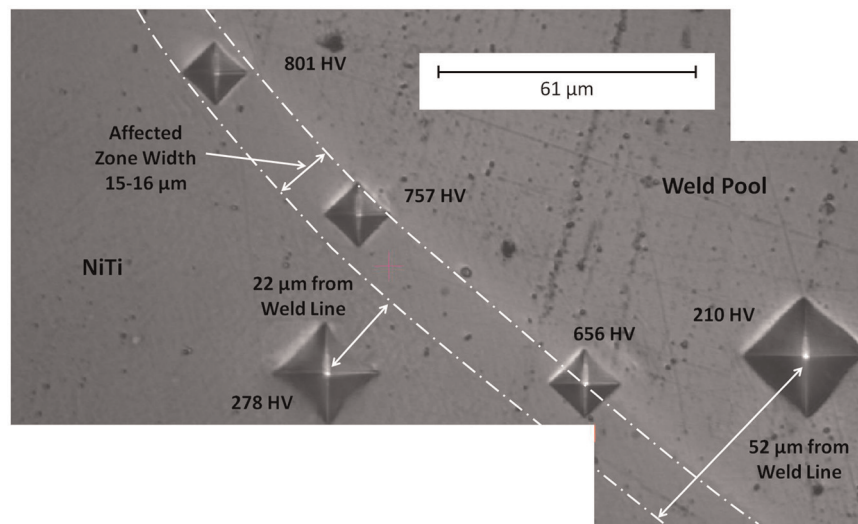

Figure 12. Composite image of individual hardness measurements in optically identified affected zone of NiTi/304 SS thick-walled specimen 2. The increased hardness is due to the formation of intermetallic compounds.
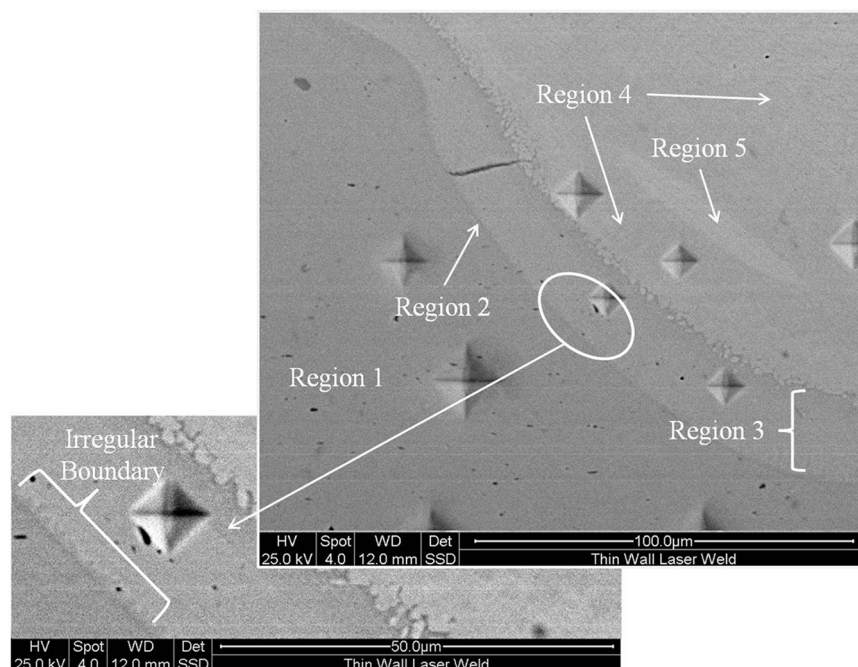

Figure 13. Image of bulk NiTi to weld metal transition in NiTi/304 SS thin-walled specimen 5.

the bulk NiTi tube, indicating that they are the same material. The difference in appearance of region 2 is attributed to two possible causes. First, the appearance is due to a change in the crystalline structure as a result of heat from the welding procedure. This would indicate that region 2 is the true HAZ in the thin-walled welds. Another possible explanation is that region 2 represents an unmixed zone, a region of molten NiTi that resolidified at the fusion boundary without mixing with the rest of the weld pool. These regions have been noted to appear in Ni-based alloys (Tillack, 1993).

If region 2 represents the HAZ in the NiTi tube, it is relatively small, 1–2 μm over most of the weld. However, if region 2 is an unmixed zone, the NiTi HAZ is bound by the 37-μm-wide area between region 2 and the individual indents shown in Figure 11. In either case, the HAZ is small compared to NiTi–NiTi laser welds reported in the literature. A particular study utilized wires of similar thickness to the wall thickness of the thin-walled samples and pulse powers similar to those in this study and found a HAZ extending approximately 300 μm beyond the fusion boundary (Tam et al., 2011). While material thickness and laser power are similar, there are several key differences that contribute to the large difference in observed HAZ widths. Where the specimen geometry of wire joints creates a one-dimensional heat flow from the weld traveling along the length of the wire, the tube joints have a significant amount of material parallel to the travel axis of the weld resulting in a larger amount of material absorbing the heat from welding. A second consideration stems from the dissimilar nature of the joints. NiTi has a relatively low thermal conductivity, $8.6 W/(m - K)$ (Johnson Matthey, 2011), when compared to Ni 200, $70 W/(m - K)$ (Mankins and Lamb,

1990), and 304 SS, $16 W/(m - K)$ (AK Steel Corporation, 2007; McGuire, 2008). The higher conductivity of the other base materials will create a preferential heat flow toward the 304 SS bulk material. Both of these considerations are the likely cause for the relatively small HAZ in the NiTi portion of the specimens.

Two individual hardness indents first presented in Figure 11 were made within region 3 with hardness values of 898 and 929 HV. The irregular boundaries between regions 2 and 3 and regions 3 and 4 are indicative of solidification nucleation sites. This shows that region 3 was liquid during part of the weld formation and thus is a partially mixed zone rather than the HAZ. Further support of this conclusion is in the compositions of region 3 relative to the bulk NiTi tube. This region has an increased Ni content compared to the as-received NiTi material, due to coalescence with the molten filler metal and, further, includes elements present in the bulk 304 SS tube. Region 3 has a composition of 59.4 at% Ni and 34.4 at% Ti, resulting in a minimum Ni-to-Ti ratio of 1.73. This ratio suggests that both Ni_3Ti_2 (Saburi et al., 1986), resulting in a 1.5 ratio of Ni to Ti, and Ni_4Ti_3 (Li et al., 2000), creating a 1.33 ratio of Ni to Ti, are likely compositions. The iron content indicates that Ti–Fe intermetallic compounds may also be present in this region. The combination of the Ni–Ti and Ti–Fe intermetallics serve to increase hardness in this region and can also act as failure initiation points, causing failure along the NiTi-weld boundary. The additional Ni content may be due to a solid solution of solidified Ni-rich filler metal and the intermetallic phases.

Region 4 has a composition of 74.1 at% Ni, 15.3 at% Ti, 7.9 at% Fe with the balance consisting of Mn and Cr. The Fe content in region 4 is nearly double that of region 3, indicating that more molten 304 SS was contributing to the formation of this region while the increased Ni content is due to an increased contribution from the Ni union. From the individual points in Figure 11, the two individual indents within region 4 and had hardness values of 521 and 451 HV. Hardness map values indicate a nominal hardness of 250–300 HV within the weld pool, indicating that region 4 is likely not representative of the entire weld pool but rather one of the multiple constituent phases. The increased hardness in this region is likely due to Ti–Fe intermetallics due to proximity with the NiTi portion of the joint. While Ti–Fe intermetallics have been shown to cause joint failure in previous studies, it appears that the Ni union has sufficiently suppressed their occurrence as to not allow for the formation of intermetallic-based cracking in the thin-walled joints.

Region 5 was found to have a significantly higher Ni content and much lower Ti content than the surrounding regions, 84.7 at% and 4.4 at%, respectively. No hardness indents were made in this region because it

Table 4. Composition of bulk base metals and transition regions in NiTi/304 SS thin-walled sample 5 and thick-walled sample 2, as shown in Figures 13 and 14.

Analysis region		Ni (at%)	Ti (at%)	Fe (at%)	Mn (at%)	Cr (at%)
Bulk NiTi		50.8	49.2	—	—	—
Bulk 304 SS		9.3	—	69.1	1.4	20.2
Thin walled	Region 1	51.0	49.0	—	—	—
	Region 2	52.0	48.0	—	—	—
	Region 3	59.4	34.4	4.1	0.6	1.5
	Region 4	74.1	15.3	7.9	0.5	2.2
	Region 5	84.7	4.4	8.1	0.4	2.4
Thick walled	Region 1	50.9	49.1	—	—	—
	Region 2	51.9	48.1	—	—	—
	Region 3	62.6	37.4	—	—	—
	Region 4	77.2	22.8	—	—	—
	Region 5	86.9	12.3	0.8	—	—

was not visible through optical means, thus the mechanical properties are unknown. However, indents made in the Ni union have typical hardness values near 150 HV, suggesting that high Ni content may cause a decrease in hardness. It is hypothesized that region 5 is representative of the lower hardness portions of the weld pool; however, additional investigation is needed to confirm this theory.

A crack in thin-walled specimen 5 is visible in region 3 (Figure 13), which is arrested at both ends at the boundary with regions 2 and 4. The crack occurs in region 3 due to the increased intermetallic formation as indicated by the higher hardness of region 3 and the composition analysis. The crack does not extend into region 2 or 4 due to their different compositions. Region 2 is similar to the NiTi base metal and region 4 has a significantly higher Ni content. In both instances, there is a lower chance of intermetallic formation. Region 4 is known to have a lower hardness than region 3, while the similarity of region 2 to the base metal also suggests lower hardness, indicating the material on either side of region 3 is more ductile, creating likely arrest points for the included crack.

A SEM image of the transition region of thick-walled sample 2 is shown in Figure 14. From the image, five distinct regions can be observed as the sample transitions from the bulk NiTi parent metal to the weld pool. Region 1 is the bulk NiTi tube and shows no discernible difference in composition from the weld boundary to the end of the tube. Region 2 is approximately 1–2 µm wide except in the region indicated, where it is 10 µm wide. Region 3 is the area observed in optical microscopy studies and shares an irregular boundary with regions 2 and 4. Region 4 has inconsistent width and is differentiated from region 5, the

primary weld pool constituent, by a lighter shaded irregular boundary.

Similar to the thin-walled analysis, the boundaries and compositions of each region were used to determine whether they comprised part of the base metal, a fusion zone, the HAZ, or weld pool. The composition results can be seen in Table 4. Regions 1 and 2 have similar composition to the bulk NiTi tube, indicating that they are the same material. The difference in appearance is due to a change in crystalline structure that likely indicates that region 2 is the true HAZ in the thick-walled welds.

Individual hardness indents first presented in Figure 12 were made within regions 3 and 4. Indents with hardness values of 801 and 757 HV were placed fully in region 3, while the indent with a hardness value of 656 HV is on the boundary separating the regions. The irregular boundaries between regions 2 and 3 and regions 3 and 4 are indicative of solidification nucleation sites. This shows that both of these regions were liquid during welding and are therefore partially mixed zones rather than part of the HAZ. Further support of this conclusion is in the compositions of each region relative to the bulk NiTi tube. Both regions have higher Ni content than the as-received NiTi material, due to coalescence with the molten filler metal. Region 3 has a ratio of 62.6 at% Ni and 37.4 at% Ti, resulting in a Ni-to-Ti ratio of 1.67. A likely composition for this region is Ni_3Ti_2 (Saburi et al., 1986), which would result in a 1.5 ratio of Ni to Ti. The additional Ni content may be due to a solid solution of Ni_3Ti_2 and solidified Ni-rich filler metal. Region 4 has a composition of 77.2 at% Ni and 22.8 at% Ti yielding a Ni-to-Ti ratio of 3.39. This region likely consists of Ni_3Ti (Bormann, 1992), a 3.00 Ni-to-Ti ratio, with the additional Ni again coming
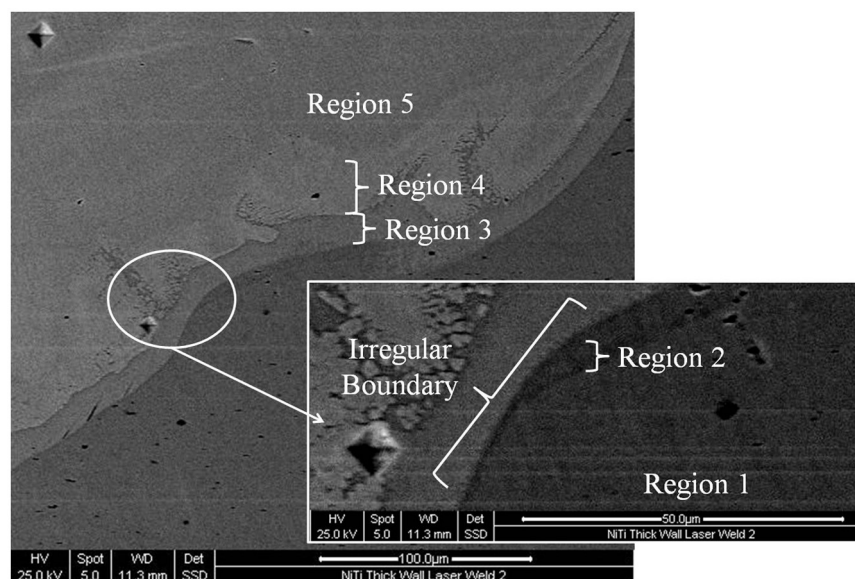

Figure 14. Composite image of bulk NiTi to weld metal transition in NiTi/304 SS thick-walled specimen 2.

from the compound being in solid solution with the filler metal. Both Ni_3Ti_2 and Ni_3Ti are intermetallic compounds that can lead to increased hardness and act as a point of weld failure when loaded. The indent observed in Figure 14 is within region 4. The hardness for this point is 634 HV, similar to the indent astride the region 3/region 4 boundary. This shows that while the compositions of the two regions are slightly different, they are both significantly harder than the bulk NiTi material.

In region 5, Fe content becomes measurable, while the Ti content drops to 12.3 at%. This, along with the irregular shape of region 5, define the region as a partially mixed zone in this analysis as Fe increases and Ti quickly decreases, indicating a shift from base metal to weld metal. However, it should be noted that this composition, unlike the other regions, is not representative of the entirety of region 5. Due to the double-bevel geometry and multipass welding procedure, the composition of the weld pool varies widely at different positions with Fe contents of some measured regions reaching over 22 at%.

Mechanical testing

Torque–angle plots for thin-walled samples 1–4 are shown in Figure 15 and for the thick-walled sample 4 in Figure 17. The ultimate torques for each sample were found and used to calculate the ultimate shear stresses in the outer fibers of the weld through $\tau = Tr_o/J$, where T is the breaking torque, r_o and r_i are the outer and inner radii, respectively, and J is the second moment of inertia given by $J = \pi/2\left(r_o^4 - r_i^4\right)$. For all specimens, the outer radius was 4.76 mm (0.1875 in). For the thin-walled specimens, the inner radius was 4.38 mm (0.1725 in), while for the thick-walled sample 4, it was 3.11 mm (0.1225 in). A summary of the ultimate torques and stresses is shown in Table 5.

Thin-walled samples 1, 2, and 4 had similar ultimate stresses, while the ultimate stress of sample 3 was significantly lower. The lower strength of sample 3 was due to the weld defects noted previously. The pinhole defects in sample 3 acted as stress concentration points and were the source of early failure. Pinhole defects are caused by contaminants on the base metal surfaces or filler metal, similar to the voids observed in the thick-walled sample. Thin-walled sample 4 was created using the same parameters as sample 3 in response to seeing the surface defects in the previous sample. Therefore, sample 3 can be treated as an outlier in considering the average strength of the thin-walled samples. The average ultimate shear strength of samples 1, 2, and 4 was 457 MPa (66.3 10^3 lbf/in^2) with a standard deviation of 30.6 MPa (4.44 10^3 lbf/in^2) and coefficient of variance of 6.7%, where coefficient of variance is calculated by $C_v = s/\bar{\tau}$, where s is the standard deviation and $\bar{\tau}$ is the average ultimate shear strength. While the small number of samples is not sufficient for a rigorous statistical analysis, these results show a low coefficient of variance, suggesting that the strength of the thin-walled specimens was not strongly affected by the variation in

Table 5. NiTi/304 SS laser weld sample strength testing results.

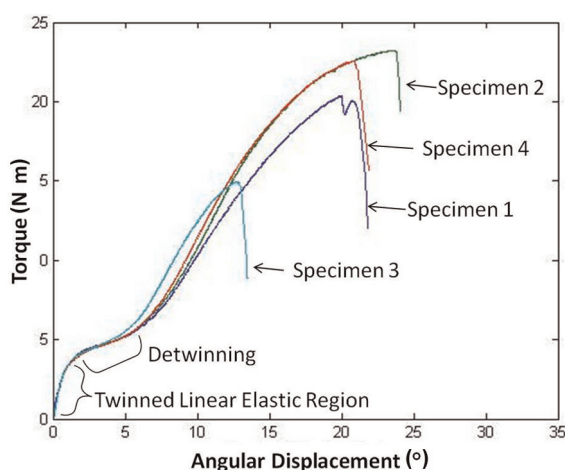| Sample	Ultimate torque, N m (in lb)	Ultimate shear stress, MPa (10^3 lbf/in^2)
Thin-walled 1	20.3 (178)	423 (61.3)
Thin-walled 2	23.2 (204)	481 (69.7)
Thin-walled 3	15.0 (132)	312 (45.3)
Thin-walled 4	22.5 (197)	467 (67.6)
Thin-walled average (1, 2, and 4)	22.0 (193)	457 (66.3)
Thick-walled 4	48.0 (422)	346 (50.2)

Figure 15. Torque–angle plots of thin-walled NiTi/304 SS samples.
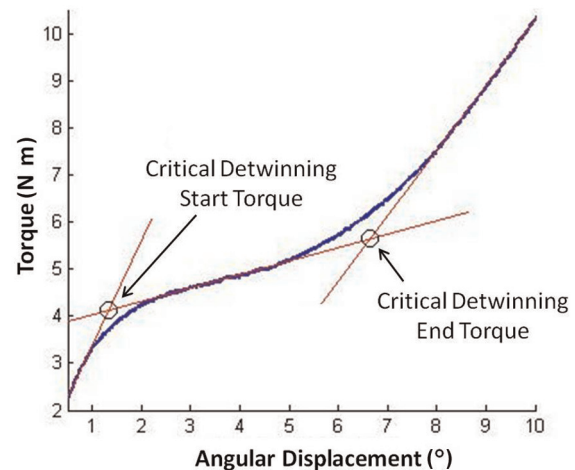

Figure 16. Example of linear fit method for finding critical detwinning torques. Data from thin-walled specimen 1.

pulse energy used in welding. A more extensive design of experiments study with multiple replicates is required to confirm this hypothesis and investigate the effects of the other weld parameters on joint strength.

The characteristic detwinning behavior of NiTi can be seen in Figures 15 and 17. Four distinct regions are present: an initially elastic region that corresponds to the linear loading of twined martensite, a detwinning region characterized by a lower torque–angle slope, a second linear elastic region corresponding to the elastic loading of detwinned martensite, and a plastic deformation region that leads to specimen failure. The detwinning plateau is characterized by a reduction in the slope of the load–displacement curve due to large deformations induced by detwinning of the martensitic crystalline structure over a relatively small range of stress.

Detwinning occurs as NiTi is loaded between its critical start and finish stresses. Using linear regression of the initial elastic region, detwinning region, and second linear region, the critical start and finish torques were found at the intersection points of the linearly extrapolated segments as illustrated in Figure 16. For the thin-walled samples, the average critical start and finish stresses were calculated from the critical torques as 82.1 MPa (11.9 10^3 lbf/in^2) and 116 MPa (16.8 10^3 lbf/in^2), respectively. There is very little variation in the critical stresses of the thin-walled specimens. A summary of the critical torques and stresses can be seen in Table 6.

Thick-walled sample 4 was mechanically tested to observe its torsional strength. Its torque–angle plot can be seen in Figure 17. It had a maximum torque of 48.0 N m (422 in lb), which corresponds to an ultimate shear strength of 346 MPa (50.2 10^3 lbf/in^2). This is slightly lower than the average shear strength found from the thin-walled tubes and is believed to be due to the presence of voids, such as those observed in the micrographs of thick-walled samples 1–3.

From Figure 17, the critical start torque was determined to be 13.1 N m (115 in lb), which corresponds to 94.5 MPa (13.7 10^3 lbf/in^2). There is no clearly defined critical finish torque due to the thick walls of the NiTi tube and the onset of plastic deformation of the 304 SS tube. The yield strength of annealed 304 SS is similar to the critical finish torque; thus, the yielding of the 304 SS tube masks the end of detwinning in the NiTi tube. In the thin-walled tubes, shear stress has very little variation through the tube wall, whereas the thick-walled tube exhibits a larger stress gradient through the tube wall. In consequence, NiTi at the outer surface may be completely detwinned, while NiTi at the inner surface of the tube may have yet to reach the critical start stress. While there may not be complete detwinning through the NiTi tube cross section, NiTi that is partially detwinned will generate recovery stresses and recover induced strain as it is heated above its austenite start temperature.

In all tests, the torsion samples failed at the weld toe on the NiTi tube. This corresponds with the location of the fusion zones observed in the micrographs. In all cases, the 304 SS tube exhibits plastic deformation, indicating that the weld strength is greater than the yield strength of the structural tube.

Fracture surface analysis

From the mechanical test results, the behavior of the joints at failure is indicative of brittle failure at the macroscale. The SEM analysis was used to observe the microscale nature of the fractures. Prior to the SEM analysis, the fracture surface of thin-walled sample 2 and all other thin-walled samples was observed to have several faceted reflective regions indicative of brittle failure within the microstructure (Mills and Davis,
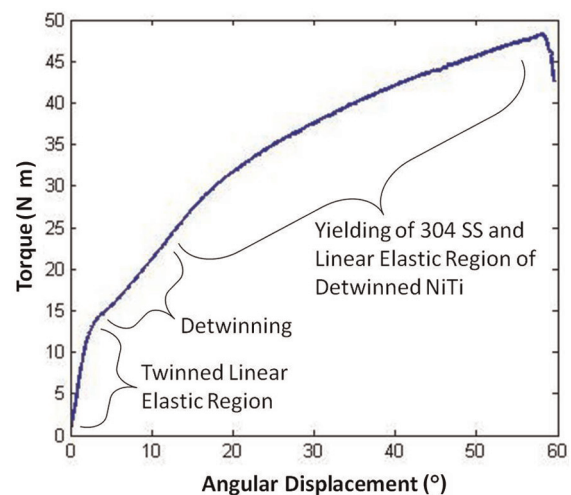
Table 6. NiTi/304 SS laser weld sample critical torques and shear stresses.

Sample	T_s^{cr}, N m (in lb)	T_f^{cr}, N m (in lb)	σ_s^{cr}, MPa (10^3 lbf/in^2)	σ_f^{cr}, MPa (10^3 lbf/in^2)
Thin-walled 1	4.12 (36.2)	5.64 (49.6)	85.0 (12.3)	116 (16.9)
Thin-walled 2	4.03 (35.4)	5.57 (49.0)	83.2 (12.1)	115 (16.7)
Thin-walled 3	3.93 (34.5)	5.67 (49.8)	81.1 (11.8)	117 (17.0)
Thin-walled 4	3.84 (33.7)	5.55 (48.8)	79.2 (11.5)	115 (16.6)
Thin-walled average	3.98 (35.0)	5.61 (49.2)	82.1 (11.9)	116 (16.8)
Thick-walled 4	13.1 (115)	—	93.9 (13.6)	—

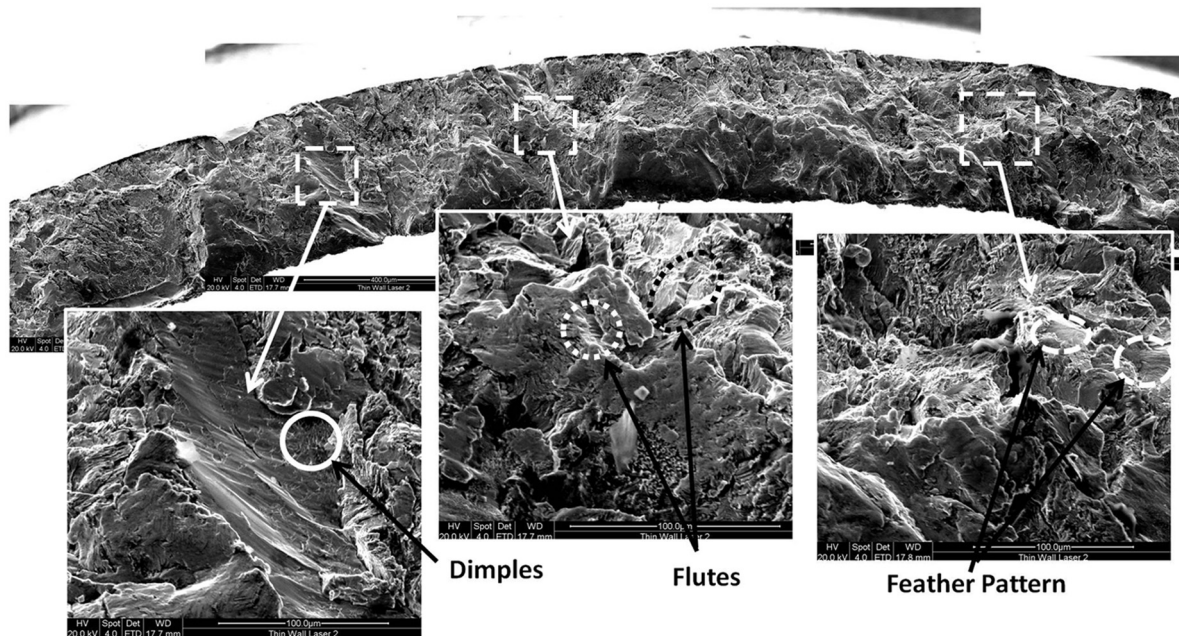**Figure 17.** Torque–angle plot of thick-walled NiTi/304 SS sample 4.

Figure 18. SEM composite image of NiTi fracture surface of thin-walled laser sample 2.
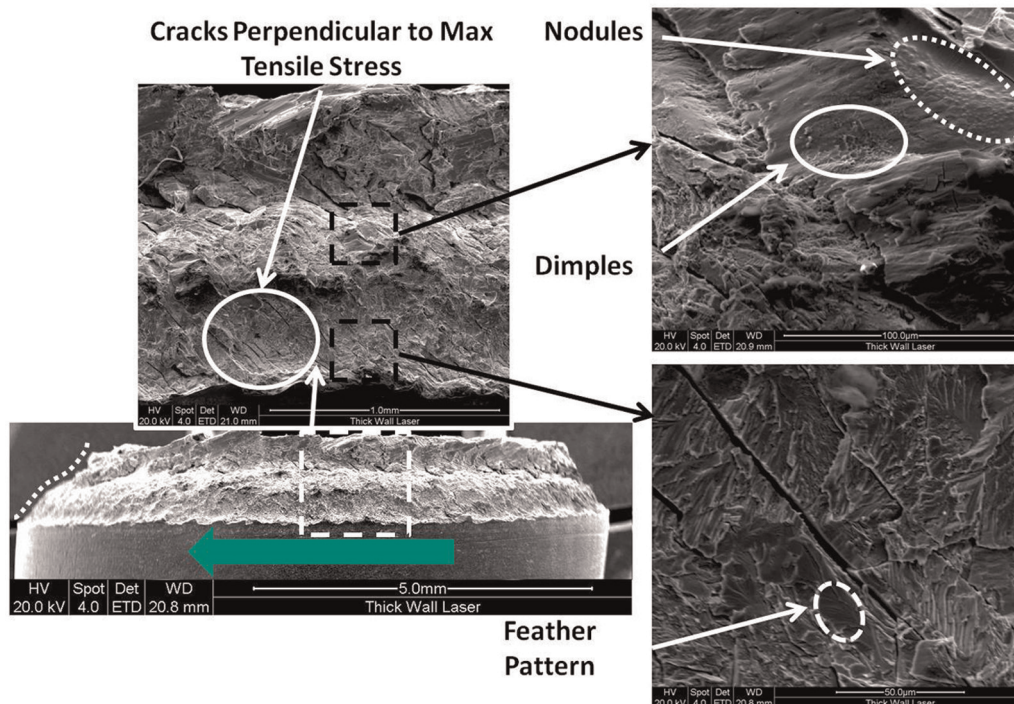SEM: scanning electron microscopy.

Figure 19. SEM images of NiTi fracture surface of thick-walled laser sample 4. The large arrow indicates the direction of rotation, whereas the dotted line highlights the fracture profile.
SEM: scanning electron microscopy.

1987). Furthermore, the profile of the fracture surface is similar to the observed fusion boundary of the cross section of thin-walled sample 5, suggesting that failure occurred due to the formation of brittle intermetallic

compounds within the optically observed partially mixed zones.

An SEM image of a representative region of thin-walled sample 2 is shown in Figure 18. A common

morphology is relatively large smooth areas with feather patterns suggesting transgranular cleavage and cleavage steps with fluted features connecting different cleavage planes. These features suggest a predominately brittle failure of the microstructure. Further evidence of the brittle nature of the joint failure is in the prevalence of cracks of different sizes as brittle failure dissipates energy by creating new surfaces via crack formation (Mills and Davis, 1987). While cracks and cleavage planes are predominant, there are regions that indicate isolated instances of ductile failure at the microlevel. The region highlighted in Figure 18 by a solid line shows a fine dimpled pattern, indicating that this area failed through microvoid coalescence.

Similar to the thin-walled specimen, the profile of the fracture surface on thick-walled sample 4 follows the fusion boundary profile observed in the sample cross sections, indicating failure occurred in the partially mixed zones likely due to the presence of intermetallic compounds. Initial unaided observation of this fracture surface reveals faceted reflective regions, as seen in thin-walled sample 2. Further support of brittle macroscale failure is seen in the fissures present in Figure 19. These large cracks are oriented approximately 45° from the axis of torsional loading. This suggests that they formed through mode I fracture along the direction of largest tensile stress, a characteristic of brittle failure (Becker, 2002). Additional regions of interest are shown in Figure 19. Similar to the thin-walled fracture surface, there is prevalence of smooth regions, feather patterns, and cleavage steps, all indicative of transgranular cleavage and brittle failure at the microlevel. Also similar to the thin-walled sample, there are isolated regions of dimples, indicating some limited failure through microvoid coalescence. An additional feature of interest is shown in Figure 19. The highlighted group of nodes may indicate a dendritic microstructure in this region (Mills and Davis, 1987); since no other instances of this morphology were encountered, it is not considered to have widespread effect on the nature of the failure mode.

Conclusion

In Part I of this two-paper study, we have studied three different laser-welded joints between NiTi and 304 SS tubes. In constructing the joints, the formation of intermetallic Ti–Fe compounds that typically cause NiTi/ferrous alloy welds to have low strength were suppressed by using Ni-rich filler metal to dilute the weld pool and prevent widespread alloying of Ti and Fe. In examining pilot joints between tubes with an outer diameter of 5.08 mm (0.200 in), it was found that increasing the pulse energy provides little increase in weld penetration but does result in an increased affected zone width. Maximum weld penetration and extension

of the affected zone in the pilot samples are $483\,\mu m$ (19.0×10^{-3} in) and $13.1\,\mu m$ (0.516×10^{-3} in), respectively.

Based on the findings from the pilot study, thin-walled NiTi and 304 SS tubes were used to make full penetration welds joining tubes with an outer diameter of 9.53 mm (0.375 in) and a wall thickness of $381\,\mu m$ (0.015 in). The thin-walled samples were used for optical microscopy, hardness studies, composition analysis, torsional testing to determine the ultimate shear strength of the welds, and analysis of the resulting fracture surfaces to determine the nature of weld failure. Optical microscopy revealed that the average affected zone extension in the thin-walled samples was $7.90\,\mu m$ (3.11×10^{-4} in). Hardness mapping and individual hardness tests indicated that outside the affected zone identified through optical microscopy, the NiTi tube remains unaffected by the laser welding process and as such should maintain its shape memory properties. Maximum observed hardness was 929 HV, which was found within the identified affected zone. Through the EDS analysis, the affected zones were determined to consist of a partially mixed zone and a region that is either an unmixed zone or the NiTi HAZ. The EDS analysis suggests that the increased hardness, found to occur within the partially mixed zone, is due to the formation of Ni-rich intermetallic compounds. Additional EDS analysis shows that the possible unmixed zone/HAZ in the thin-walled samples was typically less than $1\,\mu m$ wide. Mechanical testing results show that the average ultimate shear strength of the thin-wall welds is 457 MPa ($66.3\ 10^3$ lbf/in^2), sufficient to completely detwin the NiTi tube and plastically deform the 304 SS tube.

A multipass process was used to obtain full penetration welds between tubes with a wall thickness of 1.65 mm (0.065 in). These samples represent a significant increase in the weld depth typically observed in laser welding applications and present a method for creating structural joints of arbitrary depth while maintaining the primary benefit of laser welding: a small HAZ. While the weld sections were free of intermetallic-based cracking, there were some defects due to contaminants within the weld pool. Similar to the thin-walled tubes, an affected zone was observed in the NiTi tube that had a width of $21.9\,\mu m$ (8.62×10^{-4} in) on average. The maximum hardness measurements, up to 801 HV, were found within the identified affected zone. Hardness mapping indicated that the NiTi outside the optically observed region was unaffected by welding. The EDS analysis indicates that, similar to the thin-walled samples, the affected zone consists of partially mixed zones and either an unmixed region or HAZ. Furthermore, the increased hardness was found to coincide with the partially mixed zones and is due to the formation of intermetallic Ni–Ti compounds. Nominal widths of the unmixed zone/HAZ were found between 1 and $10\,\mu m$,

significantly smaller than the partially mixed zone. The ultimate shear strength of thick-walled specimen 4 is 346 MPa. This value is slightly lower than that observed in the thin-walled specimen but the lower strength is attributed to voids observed in the other thick-walled samples. The formation of such voids can be prevented by thorough cleaning of the base and filler metals prior to welding. The strength of the thick-walled weld was still sufficient to detwin the NiTi and cause plastic deformation of the annealed 304 SS tube.

The analysis of fracture surfaces of both thin- and thick-walled laser specimens indicate that failure occurred along the fusion boundary in the NiTi side of the weld. This suggests that the intermetallic compounds within the observed partially mixed zones served as failure initiation sites. Both samples were found to predominantly exhibit a cleavage fracture morphology consistent with transgranular fracture. This, along with the widespread cracking, is consistent with a brittle failure mode at the microscale and supports the hypothesis that brittle intermetallics were the ultimate source of failure.

The results show that laser welding is a viable process for joining NiTi to 304 SS for use in solid-state actuators. The process affects only a small amount of the joined NiTi, and with the addition of Ni-rich filler metal, eliminates cold cracking due to the formation of widespread Ti–Fe intermetallic compounds. The resulting strength of the joints is high enough to allow for the generation of blocking forces or strain recovery in the NiTi and is not the limiting factor in the joint geometries that were studied.

References

AK Steel Corporation (2007) 304/304L stainless steel. Available at: http://www.aksteel.com

Alapati S, Brantley W, Nusstein J, et al. (2006) Vickers hardness investigation of work-hardening in used NiTi rotary instruments. *Journal of Endodontics* 32: 1191–1193.

Becker WT (2002) *ASM Handbook: Volume 11—Failure Analysis and Prevention*. Materials Park, OH: ASM International.

Bormann R (1992) Ni–Ti phase diagram. Available at: http://www.asminternational.org

Cieslak MJ (1993) Cracking Phenomena Associated with Welding. *ASM Handbook: Volume 6—Welding, Brazing, and Soldering*. Materials Park, OH: ASM International, pp. 88–96.

Falvo A, Furgiuele F and Maletta C (2005) Laser welding of a NiTi alloy: mechanical and shape memory behaviour. *Materials Science and Engineering A—Structural Materials Properties Microstructure and Processing* 412: 235–240.

Gugel H, Schuermann A and Theisen WT (2006) Laser welding of NiTi wires. *Materials Science and Engineering A: Structural Materials Properties Microstructure and Processing* 481: 668–671.

Hahnlen R, Fox G and Dapino M (2012) Ultrasonic soldering of shape memory NiTi to aluminum 2024. *Welding Journal* 91(1): 1s–7s.

Hall P (1999) *Joining and Welding Nitinol*. Columbus, OH: Edison Welding Institute.

Hall P (2005) *Method of welding titanium and titanium based alloys to ferrous metals*. US Patent No. 6875949.

Hall T (1993) *Joint, a laminate, and a method of preparing a nickel-titanium alloy member surface for bonding to another layer of metal*. US Patent No. 5242759.

Hartl D, Mooney J, Lagoudas D, et al. (2008) Experimentally validated numerical analysis of aerostructures incorporating shape memory alloys. In: Dapino MJ, Zoubeida O (eds) *Proceedings of SPIE*, vol. 6929, San Diego, CA, 9–13 March 2008, pp. 692913-1–692913-11. (doi:10.1117/12.776356)

Hobart Institute of Welding Technology (2009) *Welding Guide*. Troy, OH: Hobart Institute of Welding Technology.

Johnson Matthey (2011) Nitinol technical specifications: transformation, physical, electrical, magnetic and mechanical. Available at: http://jmmedical.com

Kahn MI, Panda SK and Zhou Y (2008) Effects of welding parameters on the mechanical performance of laser welded nitinol. *Materials Transactions* 49(11): 2702–2708.

Kou S (2003) *Welding Metallurgy*. Hoboken, NJ: John Wiley & Sons, Inc.

Li B, Rong L, Li Y, et al. (2000) Fabrication of cellular Ni-Ti intermetallic compounds. *Journal of Materials Research* 15(1): 10–13.

Mabe J, Ruggeri R, Rosenzweig E, et al. (2004) Nitinol performance characterization and rotary actuator design. In: *Proceedings of SPIE* (ed EH Anderson), vol. 5388, San Diego, CA, 15–18 March 2004, pp. 95–109. (doi:10.1117/12.539008)

McGuire MF (2008) *Stainless Steels for Design Engineers*. Materials Park, OH: ASM International.

Mankins WL and Lamb S (1990) *ASM Handbook: Volume 2—Properties and Selection: Nonferrous Alloys and Special-Purpose Materials*. Materials Park, OH: ASM International.

Mills K and Davis JR (1987) *ASM Handbook: Volume 12—Fractography*. Materials Park, OH: ASM International.

Nitinol Devices & Components (2009) Material data sheet: nitinol SM495 wire. Available at: http://www.nitinol.com

Saburi T, Nenno S and Fukuda T (1986) Crystal structure and morphology of metastable X phase in shape memory Ti–Ni alloys. *Journal of the Less-Common Metals* 125: 157–166.

Tam B, Khan MI and Zhou Y (2011) Mechanical and functional properties of laser-welded Ti-55.8 Wt Pct Ni nitinol wires. *Metallurgical and Materials Transaction A: Physical Metallurgy and Materials Science* 42: 2166–2175.

Tillack DJ (1993) Selection of Nickel, Nickel-Copper, Nickel-Chromium, and Nickel-Chromium-Iron Alloys. *ASM Handbook: Volume 6—Welding, Brazing, and Soldering.* Materials Park, OH: ASM International, pp. 586–592.

US National Institutes of Health (2009) ImageJ. Available at: http://rsbweb.nih.gov/ij

Van der Eijk C, Fostervoll H, Sallom Z, et al. (2003) Plasma welding of NiTi to NiTi, stainless steel and Hastelloy C276. In: *Proceedings of ASM materials solutions*, Pittsburgh, PA, 13–15 October 2003.

Wang G (1997) Welding of nitinol to stainless steel. In: Pelton A, Hodgson D, Russell S, Duerig T (eds) *Proceedings of the international conference on shape memory and super elastic technologies, Proc. SMST-97.* Pacific Grove, CA, 2–6 March 1997, pp. 131–136, International Organization on Shape Memory and Superelastic Technologies (SMST).

Weinert K and Petzoldt V (2004) Machining of NiTi based shape memory alloys. *Materials Science and Engineering A: Structural Materials Properties Microstructure and Processing* 378: 180–184.

Wu M (2001) Fabrication of nitinol materials and components. In: Chu YY and Zhao LC (eds) *Proceedings of the international conference on shape memory and super elastic technologies.* Kunming, China, 2–6 September 2001, pp. 258–292, Trans Tech Publications Inc. Dumtem-Zurich.